

Large-Scale Mechanochemical Synthesis of Cesium Lanthanide Chloride for Radioluminescence

Tuhin Samanta,[△] Joo Hyeong Han,[△] Han Uk Lee, Bo Kyung Cha, Yong Min Park, Noolu Srinivasa Manikanta Viswanath, Han Bin Cho, Hyeon Woo Kim, Sung Beom Cho, and Won Bin Im^{*}



Cite This: *Inorg. Chem.* 2024, 63, 16483–16490



Read Online

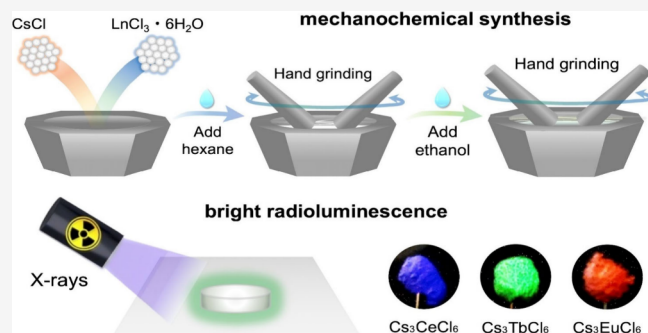
ACCESS |

Metrics & More

Article Recommendations

Supporting Information

ABSTRACT: Cesium lanthanide chloride (Cs_3LnCl_6), a recently developed class of lanthanide-based zero-dimensional metal halides, has garnered a significant amount of interest because of its potential applications in scintillators, light-emitting diodes, and photodetectors. Although cesium lanthanide chloride demonstrates exceptional scintillator properties, conventional synthesis methods involving solid-state and solution-phase techniques are complex and limited on the reaction scale. This study presents a facile mechanochemical synthesis method for producing Cs_3CeCl_6 , Cs_3TbCl_6 , and Cs_3EuCl_6 metal halides on a 5 g scale. These materials exhibit intense blue-violet, green, and red emissions upon ultraviolet excitation, with high photoluminescence quantum yields ranging from 54% to 93%. Furthermore, Cs_3CeCl_6 , Cs_3TbCl_6 , and Cs_3EuCl_6 metal halides exhibit intense radioluminescence spanning from the ultraviolet to the visible region. This research shows the potential of the scalable mechanochemical synthesis of lanthanide-based metal halides for the advancement of luminescent materials for scintillators.



INTRODUCTION

Lanthanide-based zero-dimensional (0D) metal halides have attracted a significant amount of attention because of their nontoxicity, high thermal stability, narrow emission bands, and high photoluminescence quantum yields (PLQYs). These materials have been used for light-emitting diodes (LEDs), X-ray imaging, photodetectors, and information encryption, among other applications.^{1–6} For example, Han et al. reported 0D Cs_3TbCl_6 (CTC) and Rb_3TbCl_6 (RTC) metal halides for X-ray imaging with high light yields of 56 800 and 88 800 photons/meV.¹ Cs_3CeCl_6 (CTC) single crystals were first synthesized by Seifert and co-workers.⁷ The structure of CTC was first analyzed by Mitra et al. in 1994.⁸ Subsequently, CTC metal halides were used as scintillator materials. Similarly, Cs_3EuCl_6 (CEC) was first reported by Seifert et al. in 1990.⁹ However, 0D lanthanide-based metal halides (LMHs) are generally synthesized by conventional solid-state and solution-phase methods, which are complex and limited in reaction scale.^{6,10} In this regard, mechanochemical synthesis is a promising alternative technique for the facile synthesis of LMHs.

Mechanochemical synthesis methods have attracted a considerable amount of attention because of their simple preparation of various materials.¹¹ A variety of materials, such as inorganic materials, polymers, organic metal complexes, metal halide perovskites, and luminescent metal halides, can be

synthesized via mechanochemical methods that are conventionally synthesized by solution-phase and solid-state techniques.^{12–14} The grinding or milling of two or more starting materials using a manual mortar and pestle or ball milling machine produces mechanical energy that breaks apart the starting materials for the reaction. Furthermore, the reduction in particle size induced by mechanical force continuously exposes the reactive sites of the materials.^{15,16} In specific cases, adding a small amount of solvent is advantageous for making the reaction favorable. The addition of solvents in mechanochemical synthesis is called liquid-assisted mechanochemical synthesis.^{17,18} Generally, the activation energy of these reactions is relatively low.¹⁹ The main advantages of mechanochemical synthesis are the easy implementation of the reaction, the production of a relatively small amount of side products, and a larger reaction scale compared to that of solution-phase synthesis.^{18,20}

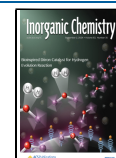
Mechanochemical synthesis has been employed for the synthesis of different transition metal chalcogenide semi-

Received: July 3, 2024

Revised: August 13, 2024

Accepted: August 16, 2024

Published: August 22, 2024



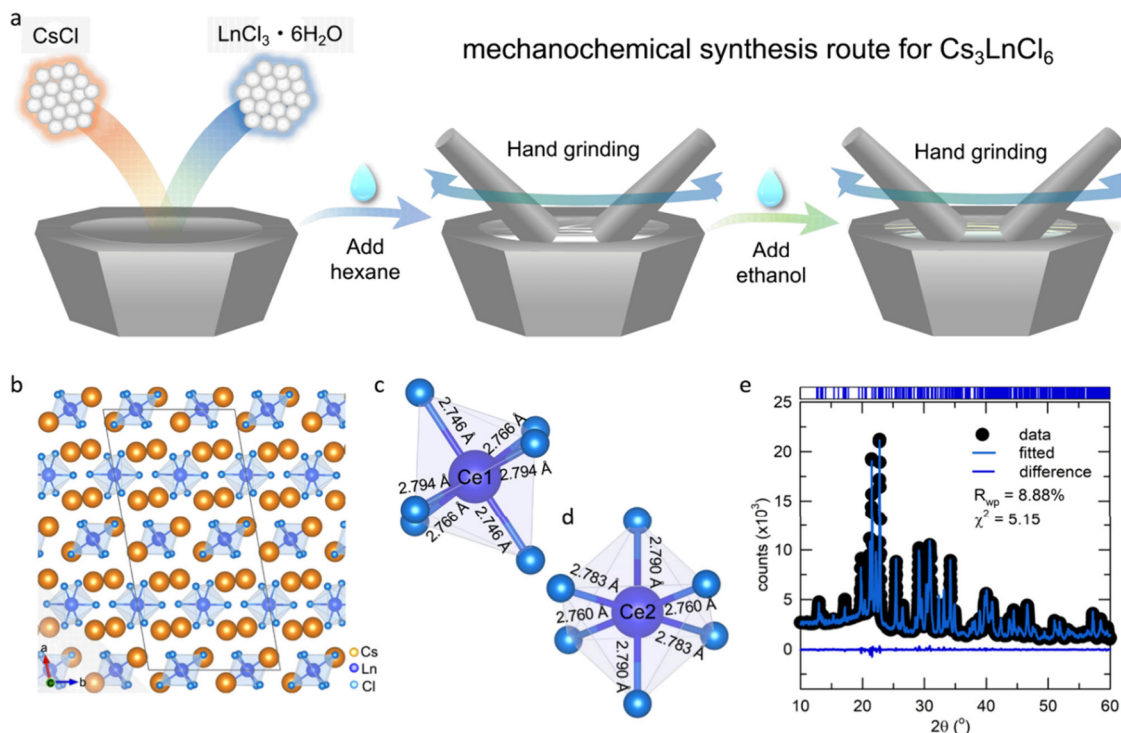


Figure 1. (a) Mechanochemical synthesis of CLnC metal halides. Structural properties of CLnC metal halides. (b) Crystal structure of CLnC in the $[010]$ direction. (c and d) Illustrations of two different octahedra of CCC metal halides. (e) X-ray powder diffraction patterns of CCC metal halides and calculated profile based on Rietveld refinement.

conductor materials.^{21,22} In recent years, it has been widely used for the synthesis of metal halide perovskites and luminescent metal halides.^{23–26} The desired metal halide perovskite can be formed by mechanical grinding of the perovskite precursors such as a monovalent cation [methylammonium (MA), formamidinium (FA), etc.] and metal halide (PbX_2 , where $\text{X} = \text{Cl}, \text{Br}$, or I).^{27–29} Hybrid perovskites, such as MAPbI_3 and FAPbI_3 , have been synthesized via mechanochemical synthesis.^{30–32} Mechanically synthesized MAPbI_3 is more pure and more thermally stable than compounds prepared by solution-based synthesis methods such as spin-coating, dip-coating, and inkjet printing.^{11,33}

This study presents the facile mechanochemical synthesis of Cs_3CeCl_6 (CCC), Cs_3TbCl_6 (CTC), and Cs_3EuCl_6 (CEC) metal halides on a 5 g scale. Upon ultraviolet (UV) excitation, CCC, CTC, and CEC metal halides exhibited intense luminescence in the UV–red region. These materials exhibited high PLQYs ranging from 54% to 93%. Furthermore, these LMHs exhibited intense blue, green, and red radioluminescence upon X-ray excitation.

EXPERIMENTAL SECTION

Materials. Cesium chloride (CsCl, 99.9%), terbium chloride hexahydrate ($\text{TbCl}_3 \cdot 6\text{H}_2\text{O}$, 99.9%), cerium chloride hexahydrate ($\text{CeCl}_3 \cdot 6\text{H}_2\text{O}$, 99.9%), europium chloride hexahydrate ($\text{EuCl}_3 \cdot 6\text{H}_2\text{O}$, 99.9%), and hexane (anhydrous, 95%) were purchased from Sigma-Aldrich. Ethyl alcohol (anhydrous, 99.9%) was purchased from Daejung. The chemicals were used without further purification.

Synthesis of Cs_3LnCl_6 ($\text{Ln} = \text{Ce}, \text{Tb}$, or Eu) Metal Halides. In a typical synthesis method, 18 mmol of CsCl and 6 mmol of LnCl_3 ($\text{Ln} = \text{Ce}, \text{Tb}$, or Eu) were placed in a porcelain mortar. The starting materials were mixed well with a pestle for 5 min. Subsequently, a few drops of hexane were added, and the mixture was further ground for 10 min. Then, 1 mL of ethanol was added to the reaction and mixture, which was ground for 15 min. Finally, Cs_3LnCl_6 metal halides were

collected in glass vials and dried at 150 °C for 2 h in a glovebox. The images of different synthesis steps are shown in Figure S1. No uncommon hazards were noted during the synthesis.

Structural and Morphological Characterizations. The structures of the as-synthesized Cs_3LnCl_6 (CLnC) metal halides were characterized by X-ray diffraction (XRD) (Miniflex 600) using a diffracted beam monochromator set for $\text{Cu K}\alpha$ radiation ($\lambda = 1.54056 \text{ \AA}$). The 2θ scan range was 10–60° with a step size of 0.01°. Structural information was derived from Rietveld refinement using the GSAS software suite.³⁴ A three-dimensional visualization system for electronic and structural analysis (VESTA)³⁵ was used to draw the crystal structures. The phase purity of the as-synthesized samples was analyzed via Rietveld refinement of the XRD results while considering a full refinement of the crystallographic and instrumental parameters in the GSAS program suite. Scanning electron microscopy (SEM) was performed by using a NOVA NANO SEM-450 instrument.

First-Principles Density Functional Theory Calculations. Density functional theory (DFT) calculations were performed by using the Vienna Ab initio Simulation Package (VASP).³⁶ The Perdew–Burke–Ernzerhof (PBE) function was used to describe the exchange-correlation energy of valence electrons.³⁷ The plane-wave cutoff energy was set to 520 eV, and the projector-augmented method was utilized.³⁸ Structural optimization was truncated after Hellmann–Feynman forces decreased below 0.001 eV/Å. The Brillouin zone was sampled using the Monkhorst–Pack method with a $1 \times 3 \times 2$ k-points grid. The valence states of each cation were as follows: 5s5p6s for Cs, 4f5s5p5d6s for Ce, 4f5s5p6s for Tb, 4f5s5p6s for Eu, and 3s3p for Cl.

Optical Characterizations. Steady-state photoluminescence (PL) spectra of the CLnC metal halides were recorded by using a Hitachi F-7000 fluorescence spectrophotometer. X-ray photoelectron spectroscopy (XPS) was performed with a Thermo Fisher Scientific (Nexsa G2) instrument. The Thermo Fisher Scientific Nexsa instrument is a fully integrated XPS instrument, with a low-power Al Kα X-ray source, 10–400 μm (can be adjusted in 5 μm steps), a 3600 mm² (600 mm × 600 mm) sample area, and a 20 mm sample thickness. The absolute PLQYs of the CLnC metal halides were

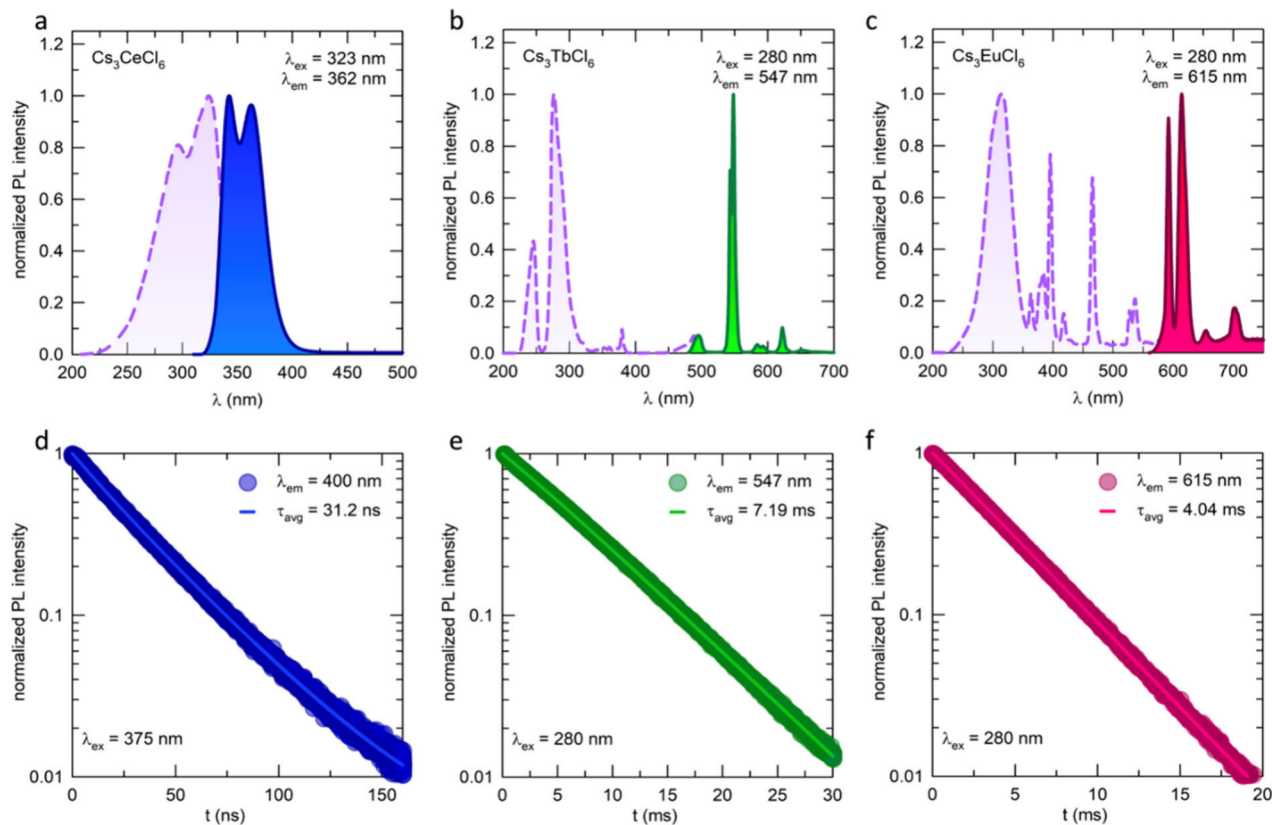


Figure 2. Optical properties of the CCC, CTC, and CEC metal halides: (a) PL and PLE of CCC, (b) PL and PLE of CTC, and (c) PL and PLE of CEC. TRPL decay curves of (d) CCC, (e) CTC, and (f) CEC.

measured using a HORIBA FluoroMax Plus spectrofluorometer paired with K-sphere petite internal, directly coupled with an integrating sphere. The excitation source was a standard 75 W xenon arc lamp, which was attached to the front of the QM sample compartment. The time-resolved photoluminescence (TRPL) of the CLnC metal halides was measured using a HORIBA spectro photo fluorometer with time-correlated single-photon counting (TCSPC) with a 371 nm (± 10 nm) pulsed LED and a 280 nm LED.

RESULTS AND DISCUSSION

This study aimed to develop an easy method for synthesizing 0D CLnC metal halides. CLnC metal halides were synthesized via a mechanochemical synthesis method on a 5 g scale. A schematic representation of the mechanochemical synthesis is shown in Figure 1a. Mechanically synthesized CLnC metal halides possess a 0D crystal structure with a monoclinic $C2/c$ space group (Figure 1b). Each Ln atom is bonded to six Cl atoms to form an octahedron. Moreover, CLnC has two distinct Ln octahedra. The two octahedra and the corresponding CCC bond lengths are shown in Figure 1c. The two distinct octahedra of CTC and CEC are shown in Figure S2. The CCC structure was analyzed by using powder XRD. XRD data were refined by using the GSAS software suite. The refined lattice parameters and atomic positions of Cs, Ce, and Cl are listed in Tables S1 and S2. The refined parameters indicated that the XRD patterns matched those of the simulated CCC metal halides. However, small CeOCl impurities were also present in the XRD pattern. The XRD pattern of the CCC is shown in Figure 1e. Similarly, the XRD patterns of the CTC and CEC metal halides were refined using the GSAS software suite, which are shown in Figures S3 and S4. The refined XRD parameters of CTC metal halides are

listed in Tables S3 and S4. Similarly, the refined XRD parameters of CEC metal halides are listed in Tables S5 and S6. Notably, CTC and CEC do not have any impurity phases. Additionally, we have included the XRD patterns of CCC, CTC, and CEC along with the standard XRD pattern shown in Figures S5–S7, respectively. The elemental analysis of CTC, CEC, and CCC was performed via XPS. The full-range XPS survey spectra exhibited distinctive peaks of Cs 3d, Tb 3d, and Cl 2p for CTC; Cs 3d, Ce 3d, and Cl 2p for CCC; and Cs 3d, Eu 3d, and Cl 2p for CEC. The XPS survey profiles of CCC, CTC, and CEC are shown in Figure S8. High-resolution XPS exhibited the characteristic peaks of Tb^{3+} , Eu^{3+} , and Ce^{3+} ions, as shown in Figure S9. XPS confirmed the presence of Tb, Ce, and Eu in the metal halides in the +3 oxidation state. After structural analysis, the morphology of the CLnC metal halides was investigated via SEM image analysis. The SEM image of the CCC demonstrated that the average particle size was $\sim 1.5 \mu\text{m}$ (Figure S10). The average particle sizes of CTC and CEC were $> 10 \mu\text{m}$, as shown in Figures S11 and S12, respectively.

The formation energies of CCC, CTC, and CEC were calculated to provide insights into the feasibility of the mechanochemical synthesis of these specific metal halides. The formation energy of a material is expressed by eq 1, where E_f is the formation energy, E_{bulk} is the total energy of the halide perovskite, and μ_i is the chemical potential of each element.

$$E_f = E_{\text{bulk}} - \sum \mu_i \quad (1)$$

The formation energies of CCC, CTC, and CEC metal halides were calculated by using eqs 2–4, respectively.

$$E_{f\text{CCC}} = E_{\text{CCC}} - 3\mu_{\text{Cs}} - \mu_{\text{Ce}} - 3\mu_{\text{Cl}_2} \quad (2)$$

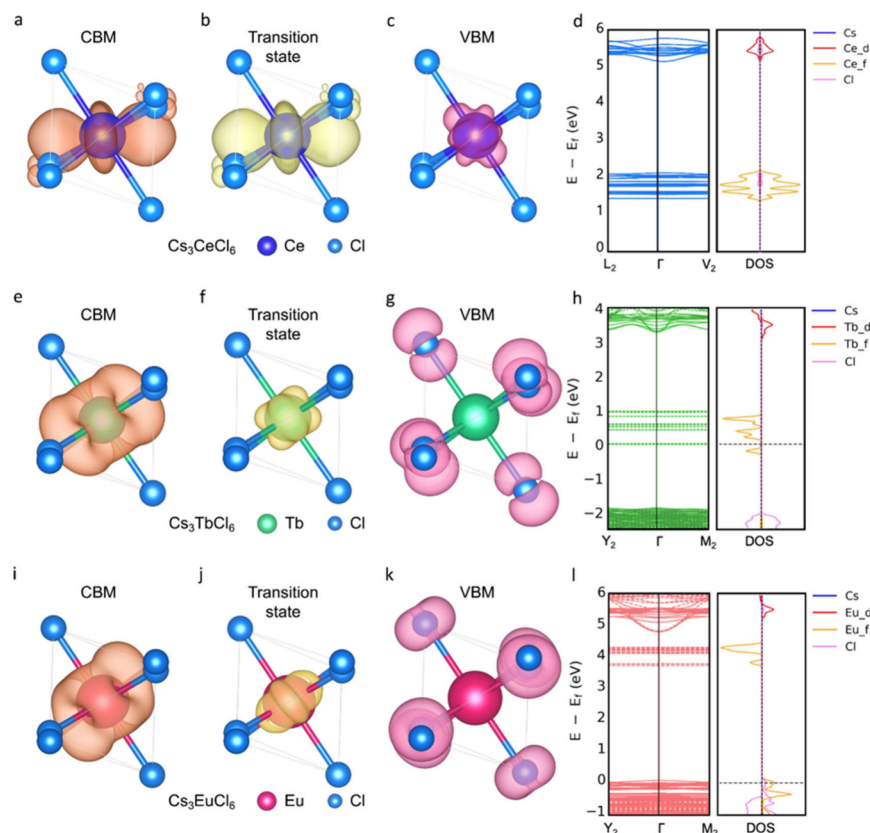


Figure 3. DFT-calculated partial charge distributions, band structures, and orbital-projected densities of states of (a–d) CCC, (e–h) CTC, and (i–l) CEC. The partial charge distributions were extracted by referring to our experimental results. For CCC, the conduction band minimum (CBM) and transition state were computed at the minimum of the 5d orbital and the valence band maximum (VBM) was computed at the maximum of the 4f orbital. For CTC and CEC, the CBM was simulated at the minimum of the 5d orbital, the transition state at the minimum of 4f orbital, and the VBM at the maximum of the Cl orbital.

$$E_{fCTC} = E_{CTC} - 3\mu_{\text{Cs}} - \mu_{\text{Ce}} - 3\mu_{\text{Cl}_2} \quad (3)$$

$$E_{fCEC} = E_{CEC} - 3\mu_{\text{Cs}} - \mu_{\text{Ce}} - 3\mu_{\text{Cl}_2} \quad (4)$$

The chemical potentials of Cs, Ce, Eu, Tb, and Cl_2 are -0.83 , -5.93 , -10.31 , -4.55 , and -3.60 eV/atom, respectively. The calculated formation energies of CCC, CTC, and CEC from these equations were -21.774 , -29.624 , and -20.456 , respectively, which are presented in Table S7. The negative formation energies of the CCC, CTC, and CEC metal halides indicate a thermodynamically favorable reaction for mechanochemical synthesis. After structural and morphological analyses, the optical properties of the CCC, CTC, and CEC metal halides were investigated. The steady-state PL and photoluminescence excitation (PLE) spectra of the CCC, CTC, and CEC metal halides were measured under ultraviolet excitation by monitoring the emission peak maxima, as shown in Figure 2. Upon excitation at 323 nm, CCC exhibits intense blue-violet luminescence with two asymmetric peaks at 380 and 409 nm, as shown in Figure 2a. The major luminescence peaks at 380 and 409 nm originated from the transition from the lowest $5d^1$ to the $4f^1$ (${}^2F_{5/2}$ and ${}^2F_{7/2}$) multiplets.³⁵ The PLE of CCC was measured by monitoring the 380 nm peak. A broad excitation band in the range of 240 – 380 nm was observed, attributed to $4f$ – $5d$ coupling. The PLQY of CCC was 58.83% upon excitation at 350 nm. The low-temperature PL of CCC was measured in the range of 100 – 275 K, as shown in Figure S13. With a decrease in temperature, the nonradiative process slowed because of the lower thermal

energy. Therefore, the PL intensity of the CCC gradually increased. Additionally, the CCC thermal stability was measured at 25 – 225 °C. With an increase in temperature, the PL intensity decreased owing to thermal quenching. The thermal stability for CCC is presented in Figure S14. Similarly, CTC exhibited bright green luminescence of Tb^{3+} ions, with peaks at 490 , 548 , 585 , and 621 nm upon excitation at 280 nm. The luminescence peaks at 490 , 548 , 585 , and 621 nm are attributed to the ${}^5D_4 \rightarrow {}^5F_6$, ${}^5D_4 \rightarrow {}^5F_5$, ${}^5D_4 \rightarrow {}^7F_4$, and ${}^5D_4 \rightarrow {}^7F_3$ transitions, respectively.³⁹ The PLE of CTC exhibited a broad band in the range of 240 – 320 nm. The broadband excitation band ranged from 240 to 320 nm, corresponding to the charge transfer band (CTB) of $\text{Cl}^- \rightarrow \text{Tb}^{3+}$, with a maximum peak at 280 nm. Narrow bands ranging from 340 to 400 nm were assigned to the spin-forbidden $4f$ – $4f$ transitions of the Tb^{3+} ions. The PLQY of CTC was 93.6% , measured at 290 nm excitation. The PL and PLE spectra of the CTC are shown in Figure 2b. The low-temperature PL of the CTC was measured in the range of 100 – 275 K. The low-temperature PL spectrum of the CTC is shown in Figure S15. With a decrease in temperature, the PL intensity of the CCC gradually increased owing to the suppression of nonradiative processes. Additionally, the thermal stability of CTC was measured in the range of 25 – 225 °C. With an increase in temperature, the PL intensity of the CTC decreased owing to thermal quenching. However, CTC retained 80% of the initial PL intensity at 225 °C, as shown in Figure S16. Figure 2c shows the PL and PLE spectra of CEC. Upon UV excitation (280 nm), CEC exhibited

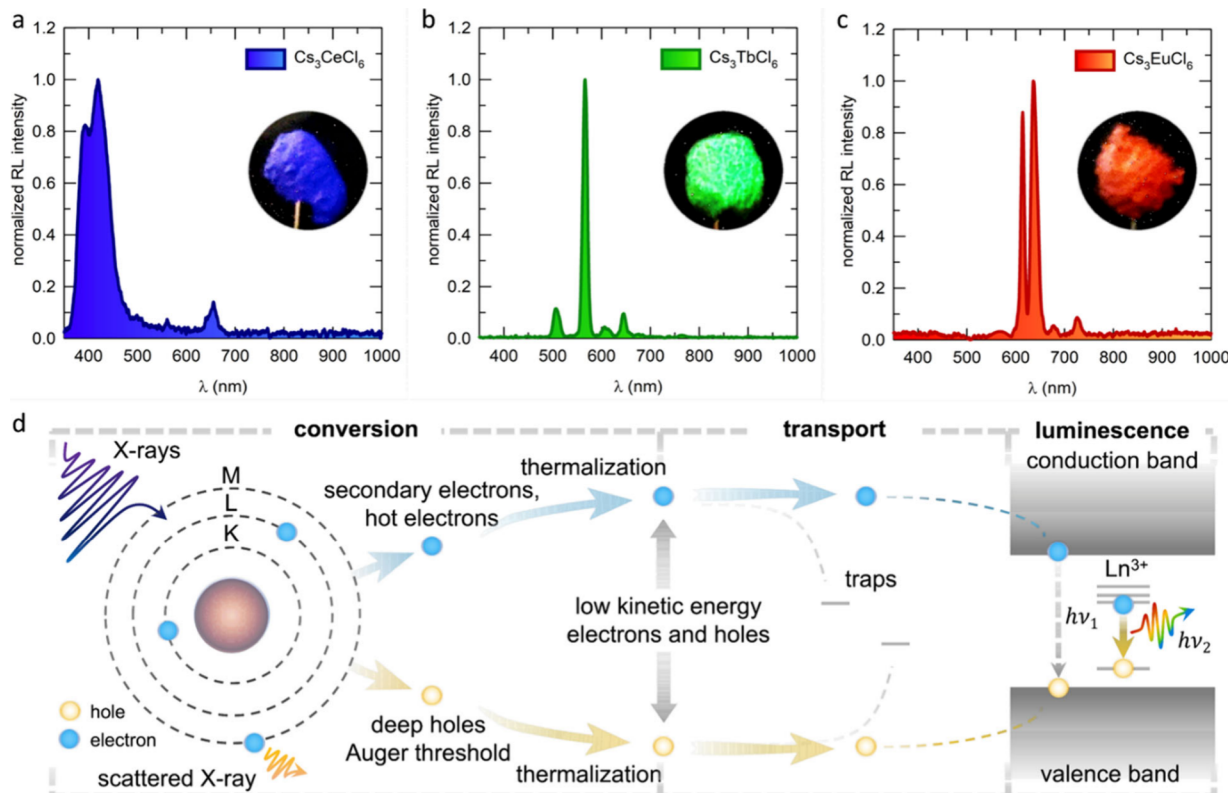


Figure 4. Radioluminescence (RL) spectra of (a) CCC, (b) CTC, and (c) CEC. The insets of panels a–c show the digital images of CCC, CTC, and CEC upon X-ray irradiation. (d) Mechanism of RL for CLnC metal halides.

an intense red luminescence in the range of 580–730 nm, with luminescence peaks at 591 nm ($^5D_0 \rightarrow ^7F_1$), 615 nm ($^5D_0 \rightarrow ^7F_2$), 650 nm ($^5D_0 \rightarrow ^7F_3$), and 700 nm ($^5D_0 \rightarrow ^7F_4$).^{40,41} The PLE of the CEC was measured by monitoring the 615 nm peak. The PLE of CEC exhibited a broad excited band in the range of 230–340 nm and narrow bands in the range of 350–530 nm. The broad excitation band originated from the $\text{Cl}^- \rightarrow \text{Eu}^{3+}$ CTB, and the narrow band originated from the 4f–4f transitions of the Eu^{3+} ions. The PLQY of the CEC was 54.8% upon excitation at 394 nm. Furthermore, the low-temperature PL of CEC was measured in the range of 100–275 K. Similar to that of CTC, the PL intensity of CEC increased with a decrease in temperature. The low-temperature PL spectrum of the CEC is shown in Figure S17. Subsequently, the thermal stability of CEC was measured, as shown in Figure S18. CEC retained 80% of its initial PL intensity at 225 °C. Time-resolved photoluminescence (TRPL) spectra of CCC, CTC, and CEC were measured by monitoring their luminescence maxima. The TRPLs of CCC, CTC, and CEC are shown in panels d–f, respectively, of Figure 2. The average lifetime of CCC was 31.2 ns. The nanosecond lifetimes of CCC originated from 4f–5d coupling. The lifetimes of CTC and CEC were 7.19 and 4.04 ms, respectively.^{1,5,42} DFT calculations were performed to understand the electronic structures of CCC, CTC, and CEC. Figure 3a–d shows the electronic schematic structures of CCC. It was found that the conduction band minimum (CBM) and transition state were significantly composed of the 5d orbitals, and the valence band maximum (VBM) was mainly composed of the 4f orbitals, with a gap between these orbitals identified as 2.892 eV. On the contrary, the electronic structures of CTC (Figure 3e–h) and CEC (Figure 3i–l) were slightly different from that of CCC,

showing that the CBM consisted of 5d orbitals, the transition state consisted of 4f orbitals, and the VBM consisted of Cl orbitals, with bandgaps of 5.006 and 4.778 eV, respectively. The influence of Cs^+ cations on the density of states was minimal. The overall partial charge distributions of CCC, CTC, and CEC are shown in Figure S19. These computations demonstrate the origin of the 5d–4f transition in Ce and the 4f–4f transition in Tb and Eu. Then, structural, optical, and theoretical studies investigated the scintillator properties of CCC, CTC, and CEC. Upon irradiation with 70 keV X-rays, CCC exhibited intense blue radioluminescence in the range of 380–500 nm through to that of PL owing to the high-energy scintillation. The radioluminescence of CCC is shown in Figure 4a. The inset of Figure 4a shows a blue image of CCC under X-ray irradiation. However, the radioluminescence of CCC is red-shifted compared to the photoluminescence spectra. The reason for this red shift was the high-energy ionization radiation that creates a quantum tunneling effect between the trap states and the conductance band.^{43,44} This tunneling effect is possible for CCC owing to their 5d–4f coupling. In the case of CTC, X-ray irradiation generated radioluminescence in the green region, with a peak maximum of 550 nm. The radioluminescence of the CTC is shown in Figure 4b. The inset of Figure 4b shows a green image of CTC under X-ray irradiation. Similarly, CEC exhibited red radioluminescence at 615 nm upon X-ray irradiation, as shown in Figure 4c. The inset of Figure 4c shows red images of CEC upon X-ray irradiation. Figure 4d demonstrates the mechanism of radioluminescence. X-ray radiation interacts with scintillator materials through various photoelectric effects, Compton scattering, Thomson scattering, and pair production. After the absorption of incident X-ray radiation by an atom, the

excited electron from the inner shell of the atom is ejected. Therefore, the atoms were ionized. This effect is dominant when the incident photon energy is <100 keV. Subsequently, hot electrons and deep holes were generated via the photoelectric effect. Furthermore, electron–electron coupling and the Auger process produce numerous secondary electrons with low kinetic energy. Subsequently, these charge carriers interact with the photons and are thermally dissipated. Numerous low-kinetic energy electrons and holes gradually accumulate in the conduction and valence bands, respectively. Notably, the entire conversion stage occurred on a subpicosecond time scale.

CONCLUSION

In summary, we used a mechanochemical synthesis method to produce 0D lead-free monoclinic CCC, CTC, and CEC metal halides. The essential advantage of this approach was its high scalability. The CCC, CTC, and CEC metal halides exhibited intense blue, green, and red luminescence, respectively, upon UV excitation. Additionally, these metal halides exhibited high PLQYs ranging from 54% to 93%. CCC, CTC, and CEC metal halides exhibited excellent scintillator properties and displayed excellent blue, green, and red luminescence upon X-ray irradiation. Thus, the mechanochemical synthesis of lanthanide-based metal halides offers new opportunities for the synthesis of metal halides and their application in radio-luminescence.

ASSOCIATED CONTENT

Data Availability Statement

Research data are not shared.

Supporting Information

The Supporting Information is available free of charge at <https://pubs.acs.org/doi/10.1021/acs.inorgchem.4c02766>.

X-ray diffraction patterns, Rietveld refinement data from the X-ray diffraction patterns, results of X-ray photo-electron spectroscopy, scanning electron microscopy images, temperature-dependent photoluminescence spectra, and partial charge distributions of the metal halides ([PDF](#))

AUTHOR INFORMATION

Corresponding Author

Won Bin Im – Division of Materials Science and Engineering, Hanyang University, Seoul 04763, Republic of Korea;
[orcid.org/0000-0003-2473-4714](#); Email: imwonbin@hanyang.ac.kr

Authors

Tuhin Samanta – Division of Materials Science and Engineering, Hanyang University, Seoul 04763, Republic of Korea

Joo Hyeong Han – Division of Materials Science and Engineering, Hanyang University, Seoul 04763, Republic of Korea

Han Uk Lee – Department of Materials Science and Engineering, Ajou University, Suwon-si, Gyeonggi-do 16499, Republic of Korea; Department of Energy Systems Research, Ajou University, Suwon 16499, Republic of Korea

Bo Kyung Cha – Precision Medical Device Research Center, Korea Electrotechnology Research Institute (KERI), Ansan 15588, Republic of Korea

Yong Min Park – Division of Materials Science and Engineering, Hanyang University, Seoul 04763, Republic of Korea

Noolu Srinivasa Manikanta Viswanath – Division of Materials Science and Engineering, Hanyang University, Seoul 04763, Republic of Korea

Han Bin Cho – Division of Materials Science and Engineering, Hanyang University, Seoul 04763, Republic of Korea

Hyeon Woo Kim – Division of Materials Science and Engineering, Hanyang University, Seoul 04763, Republic of Korea; Nano Convergence Materials Center, Korea Institute of Ceramic Engineering and Technology (KICET), Jinju 52851, Republic of Korea

Sung Beom Cho – Department of Materials Science and Engineering, Ajou University, Suwon-si, Gyeonggi-do 16499, Republic of Korea; Department of Energy Systems Research, Ajou University, Suwon 16499, Republic of Korea;
[orcid.org/0000-0002-3151-0113](#)

Complete contact information is available at:
<https://pubs.acs.org/10.1021/acs.inorgchem.4c02766>

Author Contributions

[†]T.S. and J.H.H. contributed equally to this work.

Notes

The authors declare no competing financial interest.

ACKNOWLEDGMENTS

This work was supported by the National Research Foundation of Korea (NRF), which is funded by the Korean Government (MSIT) (NRF-2020M3H4A3081792, NRF-2021M3H4A1A02049634, and NRF-2022H1D3A3A01077343).

REFERENCES

- (1) Han, J. H.; Samanta, T.; Park, Y. M.; Kim, H. J.; Manikanta Viswanath, N. S.; Kim, H. W.; Cha, B. K.; Cho, S. B.; Im, W. B. Highly Stable Zero-Dimensional Lead-Free Metal Halides for X-ray Imaging. *ACS Energy Lett.* **2023**, *8* (1), 545–552.
- (2) Han, J. H.; Samanta, T.; Cho, H. B.; Jang, S. W.; Viswanath, N. S. M.; Kim, Y. R.; Seo, J. M.; Im, W. B. Intense Hydrochromic Photon Upconversion from Lead-Free 0D Metal Halides For Water Detection and Information Encryption. *Adv. Mater.* **2023**, *35* (40), No. e2302442.
- (3) Kim, H. W.; Han, J. H.; Samanta, T.; Lee, D. G.; Jeon, D. W.; Kim, W.; Chung, Y.-C.; Im, W. B.; Cho, S. B. High-Throughput Screening on Halide Perovskite Derivatives and Rational Design of Cs₃LuCl₆. *ACS Energy Lett.* **2023**, *8* (8), 3621–3630.
- (4) Samanta, T.; Viswanath, N. S. M.; Jang, S. W.; Min, J. W.; Cho, H. B.; Han, J. H.; Im, W. B. Thermally Stable Self-Trapped Assisted Single-Component White Light from Lead-Free Zero-Dimensional Metal Halide Nanocrystals. *Adv. Opt. Mater.* **2023**, DOI: [10.1002/adom.202202744](https://doi.org/10.1002/adom.202202744).
- (5) Lee, M.; Chung, H.; Hong, S. V.; Woo, H. Y.; Chae, J. Y.; Yoon, T. Y.; Diroll, B. T.; Paik, T. Dynamically tunable multicolor emissions from zero-dimensional Cs₍₃₎LnCl₍₆₎ (Ln: europium and terbium) nanocrystals with wide color gamut. *Nanoscale* **2023**, *15* (4), 1513–1521.
- (6) Chen, J. K.; Guo, Y.; Chen, B.; Zheng, W. L.; Wang, F. Ultrafast and Multicolor Luminescence Switching in a Lanthanide-Based Hydrochromic Perovskite. *J. Am. Chem. Soc.* **2022**, *144* (48), 22295–22301.
- (7) Seifert, H. J.; Sandrock, J.; Thiel, G. Hermonical Studies on the Systems ACI/CeCl₃ (A= Na-Cs). *J. Therm. Anal.* **1986**, *31*, 1309–1318.

- (8) Mitra, S.; Uebach, J.; Seifert, H. J. ternary Chloride in the systems ACl/TbCl_3 ($\text{A} = \text{K}, \text{Rb}, \text{Cs}$). *J. Solid State Chem.* **1995**, *115*, 484–489.
- (9) Seifert, H. J.; Sandrock, J. Ternäre Chloride in den Systemen ACl/EuCl_3 ($\text{A} = \text{Na}, \text{Rb}, \text{Cs}$). *ZAAC* **1990**, *587* (1), 110–118.
- (10) Wang, L.; Guo, Q.; Duan, J.; Xie, W.; Ji, G.; Li, S.; Chen, C.; Li, J.; Yang, L.; Tan, Z.; Xu, L.; Xiao, Z.; Luo, J.; Tang, J. Exploration of Nontoxic Cs_3CeBr_6 for Violet Light-Emitting Diodes. *ACS Energy Lett.* **2021**, *6* (12), 4245–4254.
- (11) Palazon, F.; El Ajouri, Y.; Bolink, H. J. Making by Grinding: Mechanochemistry Boosts the Development of Halide Perovskites and Other Multinary Metal Halides. *Adv. Energy Mater.* **2020**, *10* (13), 1902499 DOI: [10.1002/aenm.201902499](https://doi.org/10.1002/aenm.201902499).
- (12) Tan, D.; Garcia, F. Main group mechanochemistry: from curiosity to established protocols. *Chem. Soc. Rev.* **2019**, *48* (8), 2274–2292.
- (13) Martinez, V.; Stolar, T.; Karadeniz, B.; Brekalo, I.; Uzarevic, K. Advancing mechanochemical synthesis by combining milling with different energy sources. *Nat. Rev. Chem.* **2023**, *7* (1), 51–65.
- (14) Kundu, K.; Dutta, P.; Acharyya, P.; Biswas, K. Pb-free layered all-inorganic metal halides RbSn_2Br_5 : Mechanochemical synthesis, band gap tuning, optical and dielectric properties. *Mater. Res. Bull.* **2021**, *140*, 111339–111349.
- (15) Jones, A. C.; Leitch, J. A.; Buck, S. B.; Browne, D. L. Mechanochemical techniques for the activation and use of zerovalent metals in synthesis. *Nat. Synth.* **2022**, *1*, 763–775.
- (16) DeGroot, H. P.; Hanusa, T. P. Solvate-Assisted Grinding: Metal Solvates as Solvent Sources in Mechanochemically Driven Organometallic Reactions. *Organometallics* **2021**, *40* (21), 3516–3525.
- (17) Martínez-Sarti, L.; Palazon, F.; Sessolo, M.; Bolink, H. J. Dry Mechanochemical Synthesis of Highly Luminescent, Blue and Green Hybrid Perovskite Solids. *Adv. Opt. Mater.* **2020**, *8* (4), 1901494–1901501.
- (18) Wu, H.; Chen, X.; Song, Z.; Zhang, A.; Du, X.; He, X.; Wang, H.; Xu, L.; Zheng, Z.; Niu, G.; et al. Mechanochemical Synthesis of High-Entropy Perovskite toward Highly Sensitive and Stable X-ray Flat-Panel Detectors. *Adv. Mater.* **2023**, *35* (29), 2301406–2301414.
- (19) Zhuang, T.; Lin, Y.; Jin, J.; Deng, Z.; Peng, Y.; Gong, L.; Wang, Z.; Du, K.; Huang, X. A Mechanochemically Synthesized Hybrid Bismuth Halide as Highly Efficient Red Phosphor for Blue Chip-Based WLED. *Adv. Opt. Mater.* **2023**, *11* (12), 2202951–2202959.
- (20) Chen, S.; Fan, C.; Xu, Z.; Pei, M.; Wang, J.; Zhang, J.; Zhang, Y.; Li, J.; Lu, J.; Peng, C. Mechanochemical synthesis of organo-selenium compounds. *Nat. Commun.* **2024**, *15* (1), 769–778.
- (21) Balaz, P.; Achimovicova, M.; Balaz, M.; Billik, P.; Cherkezova-Zheleva, Z.; Criado, J. M.; Delogu, F.; Dutkova, E.; Gaffet, E.; Gotor, F. J.; Kumar, R.; Mitov, I.; Rojac, T.; Senna, M.; Streletskaia, A.; Wieczorek-Ciuronam, K. Hallmarks of mechanochemistry: from nanoparticles to technology. *Chem. Soc. Rev.* **2013**, *42* (18), 7571–7637.
- (22) Wang, C.; Hill, M.; Theard, B.; Mack, J. A solvent-free mechanochemical synthesis of polyaromatic hydrocarbon derivatives. *RSC. Adv.* **2019**, *9* (48), 27888–27891.
- (23) Xu, Y.; Dong, W.; Su, P.; Lang, T.; He, H.; Jiang, H.; Jia, B.; Liu, X.; Han, T. Mn-Doped M_2CdCl_4 ($\text{M} = \text{CH}_3\text{NH}_3^+, \text{C}_2\text{H}_8\text{N}^+$, and $\text{C}_3\text{H}_{10}\text{N}^+$) Layered Hybrid Perovskite and Its Flexible Film Based on Simple Mechanochemical Synthesis. *Inorg. Chem.* **2024**, DOI: [10.1021/acs.inorgchem.3c03751](https://doi.org/10.1021/acs.inorgchem.3c03751).
- (24) Baek, K. Y.; Lee, W.; Lee, J.; Kim, J.; Ahn, H.; Kim, J. I.; Kim, J.; Lim, H.; Shin, J.; Ko, Y. J.; Lee, H. D.; Friend, H.; H, R.; Tae-Woo Lee, T. W.; Lee, J.; Kang, K.; Lee, T. Mechanochemistry-driven engineering of 0D/3D heterostructure for designing highly luminescent Cs-Pb-Br perovskites. *Nat. Commun.* **2022**, *13* (1), 4263–4274.
- (25) Viswanath, N. S. M.; Samanta, T.; Yoon, Y.; Jang, S. W.; Kim, K.; Im, W. B. Lone-Pair-Driven, Brightly Emitting Lead-Free Zero-Dimensional Inorganic Luminescent Member. *Adv. Opt. Mater.* **2024**, *12*, 2302565.
- (26) Kundu, K.; Dutta, P.; Acharyya, P.; Biswas, K. Mechanochemical Synthesis, Optical and Magnetic Properties of Pb-Free Ruddlesden–Popper-Type Layered $\text{Rb}_2\text{CuCl}_2\text{Br}_2$ Perovskite. *J. Phys. Chem. A* **2021**, *125* (8), 4720–4729.
- (27) Prochowicz, D.; Franckevičius, M.; Cieślak, A. M.; Zakeeruddin, S. M.; Grätzel, M.; Lewiński, J. Mechanosynthesis of the hybrid perovskite $\text{CH}_3\text{NH}_3\text{PbI}_3$: characterization and the corresponding solar cell efficiency. *J. Mater. Chem. A* **2015**, *3* (41), 20772–20777.
- (28) Jodłowski, A. D.; Yepez, A.; Luque, R.; Camacho, L.; de Miguel, G. Benign-by-Design Solventless Mechanochemical Synthesis of Three-, Two-, and One-Dimensional Hybrid Perovskites. *Angew. Chem., Int. Ed. Engl.* **2016**, *55* (48), 14972–14977.
- (29) Prochowicz, D.; Yadav, P.; Saliba, M.; Kubicki, D. J.; Tavakoli, M. M.; Zakeeruddin, S. M.; Lewiński, J.; Emsley, L.; Grätzel, M. One-step mechanochemical incorporation of an insoluble cesium additive for high performance planar heterojunction solar cells. *Nano Energy* **2018**, *49*, 523–528.
- (30) Hintermayr, V. A.; Richter, A. F.; Ehrat, F.; Doblinger, M.; Vanderlinden, W.; Sichert, J. A.; Tong, Y.; Polavarapu, L.; Feldmann, J.; Urban, A. S. Tuning the Optical Properties of Perovskite Nanoplatelets through Composition and Thickness by Ligand-Assisted Exfoliation. *Adv. Mater.* **2016**, *28* (43), 9478–9485.
- (31) Kubicki, D. J.; Prochowicz, D.; Hofstetter, A.; Saski, M.; Yadav, P.; Bi, D.; Pellet, N.; Lewiński, J.; Zakeeruddin, S. M.; Grätzel, M.; Lyndon, E. Formation of Stable Mixed Guanidinium-Methylammonium Phases with Exceptionally Long Carrier Lifetimes for High-Efficiency Lead Iodide-Based Perovskite Photovoltaics. *J. Am. Chem. Soc.* **2018**, *140* (9), 3345–3351.
- (32) Chen, D.; Li, J.; Chen, X.; Chen, J.; Zhong, J. Grinding Synthesis of APBx(3) ($\text{A} = \text{MA}, \text{FA}, \text{Cs}; \text{X} = \text{Cl}, \text{Br}, \text{I}$) Perovskite Nanocrystals. *ACS Appl. Mater. Interfaces* **2019**, *11* (10), 10059–10067.
- (33) Toby, B. H. EXPGUI, a graphical user interface for GSAS. *J. Appl. Crystallogr.* **2001**, *34*, 210–213.
- (34) Momma, K.; Izumi, F. VESTA 3 for three-dimensional visualization of crystal, volumetric and morphology data. *J. Appl. Crystallogr.* **2011**, *44*, 1272–1276.
- (35) Kresse, G. Efficient iterative schemes for ab initio total-energy calculations using a plane-wave basis set. *Phys. Rev. B* **1996**, *54*, 11169.
- (36) Perdew, J. P.; Burke, P.; Ernzerhof, M. Generalized Gradient Approximation Made Simple. *Phys. Rev. B* **1994**, *50*, 3865–3868.
- (37) Blochl, P. E. Projector augmented-wave method. *Phys. Rev. B. Condens. Matter.* **1994**, *50* (24), 17953–17979.
- (38) Tanner, P. A.; Mak, C. S.; Edelstein, N. M.; Murdoch, K. M.; Liu, G.; Huang, J.; Seijo, L.; Barandiaran, Z. Absorption and Emission Spectra of Ce^{3+} in Elpasolite Lattices. *J. Am. Chem. Soc.* **2003**, *125* (43), 13225–13233.
- (39) Pan, G. C.; Bai, X.; Yang, D. W.; Chen, X.; Jing, P. T.; Qu, S. N.; Zhang, L. J.; Zhou, D. L.; Zhu, J. Y.; Xu, W.; Bino, D.; Song, H. Doping Lanthanide into Perovskite Nanocrystals: Highly Improved and Expanded Optical Properties. *Nano Lett.* **2017**, *17* (12), 8005–8011.
- (40) Sarkar, D.; Meesaragandla, B.; Samanta, T.; Mahalingam, V. A Greener Approach towards Making Highly Luminescent Ln^{3+} -Doped NaYF_4 Nanoparticles with Ligand-Assisted Phase Control. *Chemistryselect* **2016**, *1* (15), 4785–4793.
- (41) Samanta, T.; Hazra, C.; Praveen, A. E.; Ganguli, S.; Mahalingam, V. Synthesis of Hexagonal-Phase Eu^{3+} -Doped GdF_3 Nanocrystals above Room Temperature by Controlling the Viscosity of the Solvents. *Eur. J. Inorg. Chem.* **2016**, *2016* (6), 802–807.
- (42) Samanta, T.; Yadav, A. N.; Han, J. H.; Kim, M.; Jang, S. W.; Viswanath, N. S. M.; Im, W. B. Cerium-Sensitized Highly Emissive 0D Cesium Cerium Terbium Chloride Alloy Nanocrystals for White Light Emission. *Advanced Optical Materials* **2024**, DOI: [10.1002/adom.202400909](https://doi.org/10.1002/adom.202400909).
- (43) Mihóková, E.; Babin, V.; Bartosiewicz, K.; Schulman, L. S.; Čuba, V.; Kučera, M.; Nikl, M. Low temperature delayed

recombination decay in scintillating garnets. *Opt. Mater.* **2015**, *40*, 127–131.

(44) Zhu, W.; Ma, W.; Su, Y.; Chen, Z.; Chen, X.; Ma, Y.; Bai, L.; Xiao, W.; Liu, T.; Zhu, H.; Liu, X.; Liu, H.; Liu, X.; Yang, Y. M. Low-dose real-time X-ray imaging with nontoxic double perovskite scintillators. *Light: Sci. Appl.* **2020**, *9* (112), 112.